

1 **Deducing non-migrating diurnal tides in the middle thermosphere**
2 **with GOLD observations of the Earth's far ultraviolet dayglow from**
3 **geostationary orbit**

4
5 Christopher S. Krier¹, Scott L. England¹, Katelynn R. Greer², J. Scott Evans³, Alan G. Burns⁴,
6 and Richard W. Eastes²

7
8 ¹Aerospace and Ocean Engineering, Virginia Polytechnic Institute and State University,
9 Blacksburg, VA, USA

10 ²Laboratory for Atmospheric and Space Physics, University of Colorado Boulder, Boulder, CO,
11 USA

12 ³Computational Physics, Inc., Springfield, VA, USA

13 ⁴High Altitude Observatory, National Center for Atmospheric Research, Boulder, CO, USA

14
15 Corresponding author: Christopher S. Krier (ckrier@vt.edu), ORCID: 0000-0002-3786-4094

16
17 **Key Points:**

- 18 i. First estimates of non-migrating diurnal tides from an observational platform in
19 geostationary orbit using GOLD.
- 20 ii. Deduction of non-migrating tides via known phase relationships between
21 temperature and composition.

22 iii. Retrieved tidal amplitudes from GOLD observations exceed their respective TIE-
23 GCM amplitudes by a factor of two in some cases.

24 **Abstract**

25 The Global-scale Observations of the Limb and Disk (GOLD) Mission images middle
26 thermosphere temperature and the vertical column density ratio of oxygen to molecular nitrogen
27 ($\Sigma\text{O}/\text{N}_2$) using its far ultraviolet imaging spectrographs in geostationary orbit. Since GOLD only
28 measures these quantities during daylight, and only over the $\sim 140^\circ$ of longitude visible from
29 geostationary orbit, previously developed tidal analysis techniques cannot be applied to the
30 GOLD dataset. This paper presents a novel approach that deduces two specified non-migrating
31 diurnal tides using simultaneous measurements of temperature and $\Sigma\text{O}/\text{N}_2$. DE3 (diurnal
32 eastward propagating wave 3) and DE2 (diurnal eastward propagating wave 2) during October
33 2018 and January 2020 are the focus of this paper. Sensitivity analyses using TIE-GCM
34 simulations reveal that our approach reliably retrieves the true phases, whereas residual
35 contributions from tides assumed to be absent, the restriction in longitude, and random
36 uncertainty can lead to $\sim 50\%$ error in the retrieved amplitudes. Application of our approach to
37 GOLD data during these time periods provides the first observations of non-migrating diurnal
38 tides in measurements taken from geostationary orbit. We identify discrepancies between
39 GOLD observations and TIE-GCM modeling. Retrieved tidal amplitudes from GOLD
40 observations exceed their respective TIE-GCM amplitudes by a factor of two in some cases.

41

42 **Plain Language Summary**

43 The uppermost region of the Earth's atmosphere, known as the thermosphere (~ 80 - 600
44 km altitude), is connected to the lowermost region by planetary-scale atmospheric waves, called

45 non-migrating tides, which are thermally driven and do not follow the apparent motion of the
46 Sun across the sky. Understanding non-migrating tides is essential to describing the global
47 dynamics of the Earth's upper atmosphere. There is a gap in observations of these waves in the
48 middle thermosphere temperature, around 150 km altitude. The NASA/GOLD instrument, in
49 geostationary orbit above the mouth of the Amazon River, images the temperature and
50 composition of the middle thermosphere. Conventional tidal analysis techniques cannot be
51 applied to the GOLD dataset, so we have designed a novel technique that infers important tides
52 using simultaneous measurements of temperature and composition. For two separate time
53 periods, we apply our technique to simulated observations and actual GOLD data. We find that
54 our technique generally infers the most important tides in simulated data with high accuracy.
55 The GOLD data reveal valuable observations of tides in the middle thermosphere as well as
56 discrepancies with the simulated data.

57

58 **1) Introduction**

59 The temperature and composition of the middle thermosphere change drastically with
60 altitude. The neutral temperature increases sharply with altitude while the density of neutral
61 constituents tends to decrease exponentially according to their respective scale heights (as well
62 as the production and loss mechanisms for certain species). Atomic oxygen and molecular
63 nitrogen are the two main constituents of this region. The vertical column density ratio of these
64 two ($\Sigma O/N_2$) is a sensitive measure of thermosphere composition. Any upward propagating
65 waves present in the mesosphere/lower thermosphere (MLT) can impact middle thermosphere
66 temperature and composition structures. A subset of thermal atmospheric tides, including some
67 non-migrating components, are generated in the troposphere and have long enough vertical

68 wavelengths to penetrate the thermosphere (Hagan et al., 2002). Decades of space-based
69 measurements have shown that the upper atmosphere owes a significant amount of its
70 longitudinal variability to non-migrating tides (e.g., Forbes et al., 2003, 2008; García-Comas et
71 al., 2016; Häusler & Lühr, 2009; Lieberman et al., 1991, 2013; Oberheide et al., 2002).

72 Thermal atmospheric tides are persistent planetary-scale waves in the neutral atmosphere
73 which are principally forced by absorption of solar radiation. They have components which have
74 periods that are subharmonics of a solar day and zonal wavelengths that are integer fractions of
75 circles of constant latitude. Non-migrating diurnal tides are the non-Sun-synchronous
76 components that have periods equal to a solar day. These tidal components induce longitudinal
77 and local time perturbations in the thermosphere-ionosphere system, and it has been shown that
78 some of the most prominent are forced by latent heat release from deep tropical convection in the
79 equatorial troposphere (Hagan et al., 2007). Additional sources of these waves in the
80 thermosphere include, but are not limited to, changes in solar radiation absorption by the
81 troposphere (Zhang et al, 2010a), wave-wave interactions (Forbes et al., 2006), and magnetic
82 field influences (Jones et al., 2013). Non-migrating diurnal tides perturb the MLT neutral
83 temperature (Zhang et al., 2006), thermospheric wind (Liebermann et al., 2013), neutral
84 composition (Oberheide et al., 2013), and significantly modify the ionosphere (England et al.,
85 2012; Immel et al., 2006). Accurate characterization of non-migrating tides is required to
86 establish agreement between modeled and observed longitudinal variations of thermosphere
87 dynamics (Ward et al., 2010). The naming convention of tidal components used in this paper is
88 as follows. The name of a tidal component begins with its period: (D = diurnal, S = semidiurnal,
89 T = terdiurnal), followed by its horizontal propagation direction: (E = eastward, W = westward,
90 no letter included in the case of stationary wave), and ends with its zonal wavenumber in the

91 universal time frame. For example, DE3 is the tidal component that propagates eastward with
92 diurnal period and zonal wavenumber 3 and S0 is the stationary semidiurnal component.
93 Longitudinal oscillations caused by non-migrating diurnal tides can be found in various
94 atmospheric fields observed by spacecraft. The global longitude coverage afforded by
95 continuous datasets collected by low Earth orbiting satellites enables the decomposition of
96 observed tides into zonal wavenumbers. Analysis of temperature observations collected by the
97 Sounding of the Atmosphere using Broadband Emission Radiometry (SABER) instrument,
98 onboard the Thermosphere Ionosphere Mesosphere Energetics and Dynamics (TIMED) satellite
99 in low Earth orbit, has elucidated the climatology of tides in the MLT region (Forbes et al., 2008;
100 Zhang et al., 2006). Non-migrating tides have been characterized in zonal wind at 400 km as
101 observed by the Challenging Minisatellite Payload (Haüsler and Lühr, 2009) as well as near 260
102 km by the Gravity Field and Steady-State Ocean Circulation Explorer (Gasperini et al., 2015).
103 Consequently, the tidal spectrum of the MLT is well-understood on climatological timescales
104 and there is some knowledge of tides at the upper thermosphere. However, there exists a gap of
105 understanding of tidal temperature dynamics in the lower and middle thermosphere. Up to now,
106 empirical modeling, namely, the Climatological Tidal Model of the Thermosphere (CTMT), has
107 been used to extend MLT temperature tides to the middle thermosphere (Oberheide et al., 2011).

108 Recently, Nischal et al. (2019) diagnosed non-migrating tides in nitric oxide $5.3 \mu\text{m}$ and
109 carbon dioxide $15 \mu\text{m}$ infrared cooling rates between 100 and 150 km as measured by SABER.
110 Infrared cooling rate tides derived from SABER are a sensible proxy for tidal activity in middle
111 thermosphere temperature. However, characterization of tides in middle thermosphere
112 temperature has not been done heretofore due to the absence of global-scale systematic
113 measurements.

114 Tidal features are expected to be prominent in spacecraft measurements of daytime
115 $\Sigma\text{O}/\text{N}_2$, but such variations have not yet been fully explained at all local times (He et al., 2010;
116 Kil et al., 2013). As discussed in Cui et al. (2014), the linearized continuity equation for plane
117 wave perturbations in the absence of rapid diffusion and in the long-wavelength limit takes the
118 form:

$$119 \quad \frac{\tilde{\rho}_i}{\bar{\rho}_i} = \frac{j\tilde{w}}{\omega H_i}, \quad (1)$$

120 Where $\tilde{\rho}_i/\bar{\rho}_i$ is the relative density perturbation corresponding to species i , \tilde{w} is the vertical wind
121 perturbation, ω is the wave period, H_i is the species-dependent scale height, and j is the
122 imaginary unit. Therefore, atomic oxygen and molecular nitrogen respond differently according
123 to their respective scale heights. Modification of the distribution of atomic oxygen and
124 molecular nitrogen in the thermosphere is one pathway through which tides can modify the
125 ionosphere (England et al., 2010) since the ion production rate is proportional to $[\text{O}]$ while
126 ionosphere loss is proportional to $[\text{N}_2]$. Analysis of TIMED/GUVI data (He et al., 2010)
127 revealed unexpected wavenumber-4 longitudinal signatures in $\Sigma\text{O}/\text{N}_2$ which remained stationary.
128 This contradicts the expectation from previous tidal observations that wavenumber-4 variations
129 propagate eastward because the DE3 amplitude in the middle thermosphere is much larger
130 ($\sim 20\%$) than that of the stationary planetary wave-4 (England et al., 2010; Hagan et al., 2009;
131 Häusler et al., 2010). Kil and Paxton (2011) and Kil et al. (2013) proposed that 135.6 nm
132 emissions originating from O^+ radiative recombination in the ionosphere contribute more to the
133 tidal variations in the derived $\Sigma\text{O}/\text{N}_2$ as compared to contributions from emissions due to
134 photoelectron impact in the middle thermosphere. In Appendix: Assessing the Impact of
135 Ionospheric Contamination, we discuss possible ionospheric signatures in the GOLD
136 measurements of $\Sigma\text{O}/\text{N}_2$ used in this work.

137 The importance of properly characterizing troposphere-thermosphere tidal coupling has
138 partially motivated the dedication of several novel spaceflight missions designed to investigate
139 the thermosphere and ionosphere from Earth orbit. The NASA Global-scale Observations of the
140 Limb and Disk (GOLD) mission has been imaging neutral temperature and $\Sigma\text{O}/\text{N}_2$ from
141 geostationary orbit since October 2018 (Eastes et al., 2020). The global and continuous
142 sampling afforded by GOLD allows for the study of tides at periods much shorter than the
143 precession period of a low Earth orbiting spacecraft. However, the GOLD instrument only
144 samples on the dayside disk within its field-of-regard. Therefore, the full tidal spectrum cannot
145 be extracted from the GOLD dataset.

146 The purpose of this paper is to (1) describe a novel approach to deducing non-migrating
147 diurnal tides using observations of far ultraviolet dayglow from geostationary orbit and (2)
148 present first results from application of the approach to GOLD data. This paper is organized as
149 follows. Section 2 describes the GOLD and TIEGCM datasets used in this work. Section 3
150 provides an explanation of the non-migrating diurnal tide retrieval algorithm. Section 4 presents
151 tests of the method on simulated GOLD data as well as the first tides retrieved from GOLD data
152 during two seasons, focusing on DE3 and DE2. Section 5 gives a summary and conclusions.

153

154 **2) Data**

155 **2.1 GOLD Dayside Disk Observations**

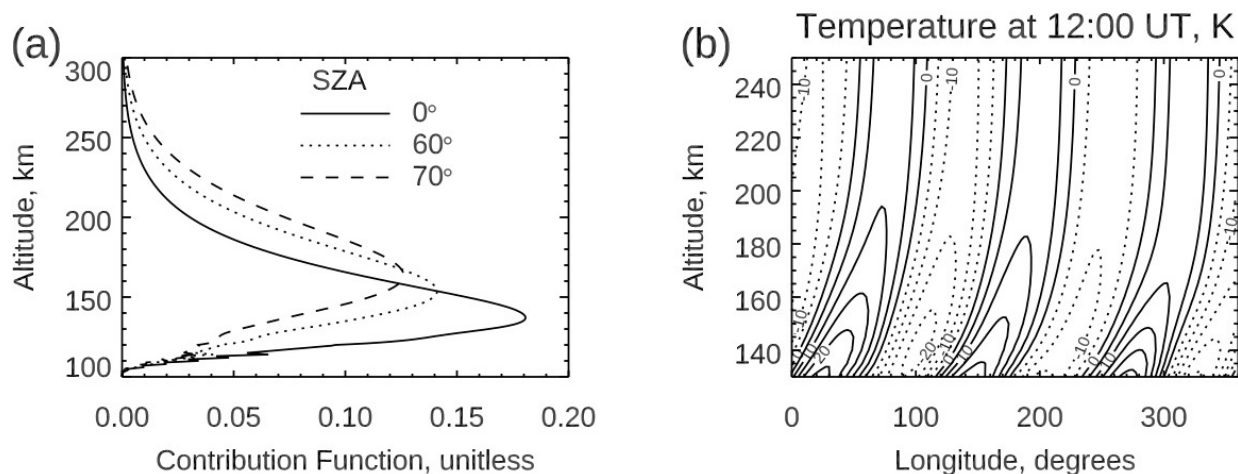
156 The GOLD mission employs two identical far ultraviolet imaging spectrographs onboard
157 the SES-14 telecommunications satellite in geostationary orbit at 47.5° West (McClintock et al.,
158 2020a; McClintock et al., 2020b). From geostationary orbit, GOLD has the advantage of being
159 able to separate spatial and temporal variations as well as image the Earth without being

160 contaminated by the South Atlantic Anomaly. The two identical and independent channels (A
161 and B) of the GOLD instrument measure emissions from ~ 132 to 162 nm of the limb and disk in
162 its field-of-regard which encompasses much of North and South America, the Atlantic Ocean,
163 and West Africa. GOLD performs dayside disk scans ~ 68 times each day at 30-minute cadence.
164 The northern and southern hemispheres are scanned separately.

165 GOLD infers disk neutral temperature from the rotational structure of N_2 LBH band
166 system emissions, $\sim 2/3$ of which comes from within one scale height of the altitude of peak
167 emission near 150 km. The GOLD disk neutral temperature is thus an effective, column
168 integrated quantity that is weighted heavily by the peak of the N_2 LBH volume emission rate
169 (photons $cm^{-3} s^{-1}$). Since the peak altitude of emission increases with solar zenith angle (SZA)
170 and neutral temperature increases rapidly with height, there is a weak ($<20\%$) dependence of the
171 GOLD effective temperature on SZA, particularly above $\sim 60^\circ$. GOLD infers $\Sigma O/N_2$ from atomic
172 oxygen 135.6 nm and molecular nitrogen LBH band emissions (Correira et al., 2020). Disk
173 temperature and $\Sigma O/N_2$ are not retrieved when the SZA is greater than 80° or the view angle from
174 local nadir, referred to as the emission angle, is greater than 75° .

175 From geostationary orbit, GOLD provides new opportunities to investigate the impacts of
176 neutral dynamics (Oberheide et al., 2020) and geomagnetic activity (Cai et al., 2020; Cai et al.,
177 2021) on thermospheric composition. One of the primary scientific objectives of the GOLD
178 mission is to determine the significance of tides propagating from below on the thermospheric
179 temperature structure (Eastes et al., 2017). This work addresses this objective by deducing non-
180 migrating diurnal tides in the combined temperature-composition dataset from GOLD. In the
181 following, we use GOLD Level 2 TDISK and ON2 data products, Version 3, which both use

182 channel A exclusively and contain images with data reported at 52 longitudes and 46 latitudes
183 (250 x 250 km² resolution at nadir).



184
185 **Figure 1.** (a) Contribution function used in the computation of effective neutral temperature, at
186 three select solar zenith angles and nadir viewing. (b) TIE-GCM non-migrating diurnal
187 temperature field as a function of altitude and longitude at 12:00 UT during October.

188

189 2.2 GOLD Observational Filter

190 The NCAR Thermosphere Ionosphere Electrodynamics General Circulation Model (TIE-
191 GCM) is a nonlinear, three-dimensional representation of the coupled thermosphere-ionosphere
192 system (Maute et al., 2017). TIE-GCM is used in this work because it provides all the
193 parameters needed to simulate the tides in GOLD dayside disk observations. Much work has
194 been done to analyze and validate tides as lower boundary forcing in TIE-GCM (Chang et al.,
195 2013; Jones et al., 2014; Pedatella et al., 2011). The TIE-GCM output used in this work has 10-
196 minute temporal resolution and 2.5° × 2.5° spatial resolution. The 10.7 cm solar radio flux was
197 set to 70 sfu. The lower boundary, at approximately 97 km, is perturbed by tides from the
198 Global Scale Wave Model (Hagan et al. (2002); see also Zhang et al. (2010b) and references

199 therein) thereby representing propagation of tides from below. As a model of disk neutral
 200 temperature, we calculate effective neutral temperature expressed as:

$$201 \quad T_n^{eff}(\lambda) = \frac{\int j(s)e^{-\tau(s,\lambda)}T_n(s)ds}{\int j(s)e^{-\tau(s,\lambda)}ds} \quad (2)$$

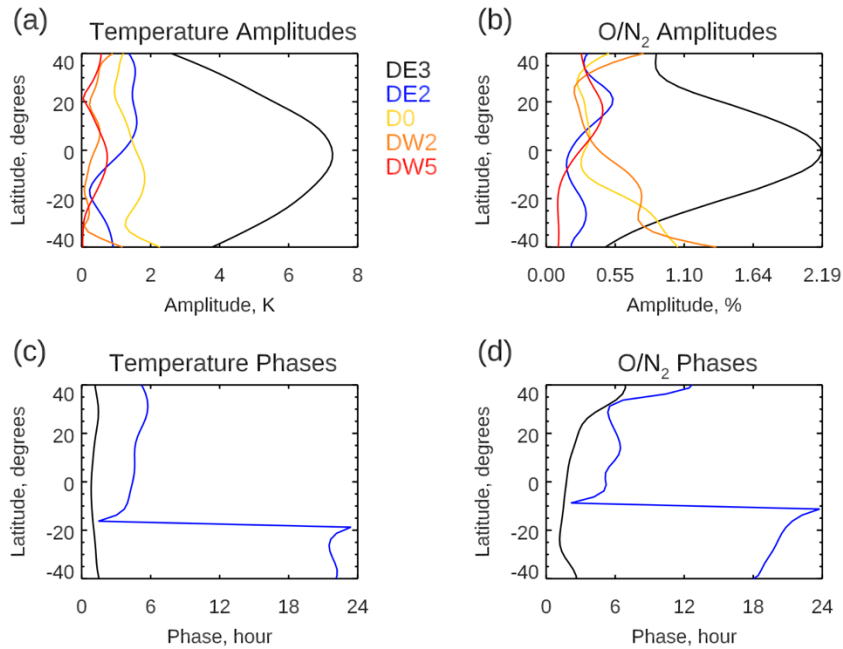
202 Where s is the slant path distance from the spacecraft (cm), j is the N₂ LBH volume emission
 203 rate (photons cm⁻³ s⁻¹), τ is the wavelength dependent slant optical depth due to absorption by
 204 molecular oxygen, and T_n is the neutral temperature (K). For our calculations of effective
 205 temperature, we define j as that of the N₂ LBH (2,0) band at 138.3 nm. Eqn. 2 can be rewritten
 206 as:

$$207 \quad T_n^{eff}(\lambda) = \int C(s, \lambda)T_n(s)ds \quad (3)$$

208 Where $C(s, \lambda)$ is a normalized emission rate profile called the contribution function which
 209 weights the neutral temperature profile. The contribution function, whose altitude dependence
 210 changes with solar zenith angle and emission angle (EMA), maximizes at the altitude of peak
 211 LBH emission rate.

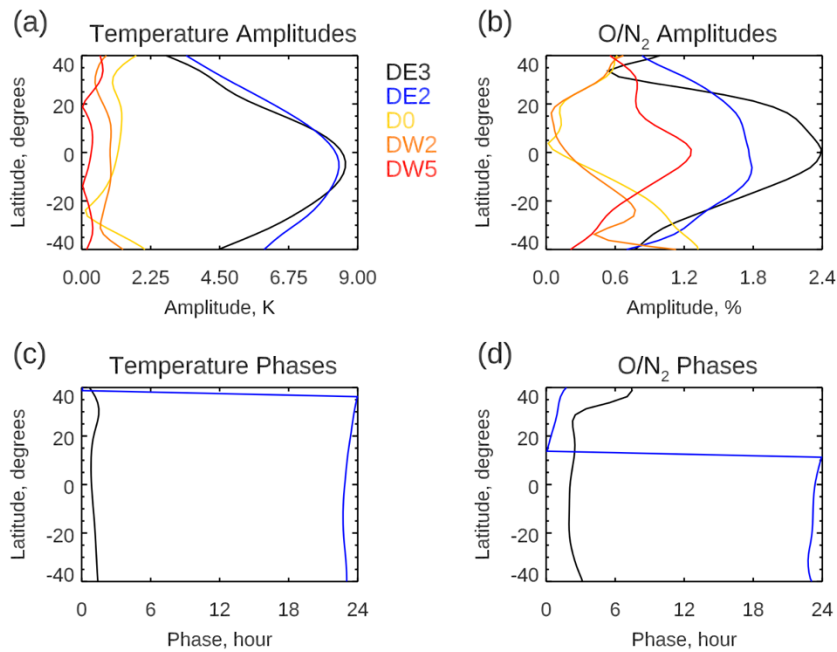
212 Figure 1a shows the contribution function for nadir viewing (EMA = 0°) and for three
 213 select solar zenith angles: 0°, 60°, and 70°. Figure 1b presents the TIE-GCM neutral temperature
 214 non-migrating diurnal field as a function of altitude and longitude at 12:00 UT during October.
 215 There is a clear wavenumber-3 pattern and eastward phase progression up to a certain altitude, ~
 216 180 km, above which amplitudes and phases settle to roughly constant values as molecular
 217 diffusion becomes dominant. This pattern indicates the DE3 tide. The temperature amplitude of
 218 the tides at the altitude of the peak emission is on the order of 10 K, but the effective temperature
 219 amplitude is necessarily lower since a band of altitudes, over which tidal phase varies, is
 220 sampled. For our purposes, we keep the viewing geometry angles constant at SZA = 70° and
 221 EMA = 0°. This is justified because (1) our approach (discussed in Section 3) uses data at SZA

222 $\sim 70^\circ$, (2) the contribution function depends weakly on EMA at high SZA, and (3) allowing SZA
223 to vary would lead to distorted tides due to SZA effects. To compute $\Sigma\text{O}/\text{N}_2$ from TIE-GCM, we
224 define the vertical O column densities relative to a standard reference N_2 depth of 10^{17} cm^{-2}
225 (Strickland et al., 1995). The non-migrating diurnal tidal phases that are used as *a priori*
226 information in our approach (see Section 3) are computed as a function of latitude and month
227 using two-dimensional fast Fourier transforms. Figure 2 presents the latitudinal structure of
228 select non-migrating diurnal tides in effective neutral temperature and $\Sigma\text{O}/\text{N}_2$ during October and
229 solar minimum conditions according to TIE-GCM. Temperature amplitude is presented in units
230 of Kelvin and $\Sigma\text{O}/\text{N}_2$ amplitude is expressed as percent deviation from the daytime zonal mean at
231 each latitude. Phase is presented as the universal time of maximum at 0° longitude. The same
232 representations of amplitude and phase are used throughout this paper. DE3 is the dominant tide
233 during October. Figure 3 is the same as Figure 2 but for January and solar minimum conditions.
234 In January, DE3 and DE2 are the two leading components in the non-migrating diurnal spectrum.
235 In Section 4.1, we use a simulated GOLD dataset to test the sensitivity of our approach to
236 random noise and aliasing. We simulate GOLD images of neutral temperature and $\Sigma\text{O}/\text{N}_2$ by
237 projecting the 24-hour, full global coverage, TIE-GCM model output onto the disk in the GOLD
238 field-of-regard. This is done through a geolocation algorithm that determines the perimeter of
239 the disk in GOLD's field-of-regard. Only model grid points inside this perimeter are sampled for
240 our analysis and, consistent with GOLD data products, we restrict data to $\text{SZA} < 80^\circ$ and
241 $\text{EMA} < 75^\circ$.



242

243 **Figure 2.** TIE-GCM non-migrating diurnal tidal amplitudes and phases as a function of latitude
 244 for effective neutral temperature, (a) and (c), and column O/N₂ ratio, (b) and (d), during October
 245 and solar minimum conditions.



246

247 **Figure 3.** Same as Figure 2 but for January.

248 **3) A Novel Approach to Deducing Non-Migrating Diurnal Tides**

249 The algorithm used in this work deduces the dominant, non-migrating diurnal tides in the
250 combined temperature-composition dataset from GOLD. The algorithm products are tidal
251 amplitudes and phases as functions of latitude for two specified non-migrating diurnal
252 components. In this section, we will describe the case of deducing the DE3 and DE2 tides
253 during October to provide an overview of the procedure. Deducing other tides during other
254 seasons follows a similar approach (shown in Section 4.2). The algorithm assumes that the non-
255 migrating diurnal variations are composed of two tidal components: DE3 and DE2, in this case.
256 The validity of this assumption is discussed in Section 4.1. A constraint on the temperature-
257 composition phase differences enforces consistency between the deduced temperature and
258 composition tides whose phase relationship depend on the horizontal wavelength and direction of
259 zonal propagation (Eqn. 4). Our algorithm makes the additional assumption that the zonal mean
260 of the dusk – dawn difference is correct despite the incomplete longitude coverage. We have
261 found that the DE3 amplitude bias introduced by limited longitude sampling is on average less
262 than 2% for October and depends on the DE3 phase. For January, we found that the bias in the
263 maximum deviation of the non-migrating diurnal proxy is on average less than 5% and depends
264 on the tidal phases of DE3 and DE2.

265 This work follows in the long tradition of inferring diurnal tides from 12-hour differences
266 (Brownscombe et al., 1985; Hitchman and Leovy, 1985; Lieberman et al., 1991, 2004, 2013;
267 Oberheide et al., 2002; Wallace and Hartranft, 1969; Wallace and Tadd, 1974; Ward et al.,
268 1999). For our approach, a proxy for the non-migrating diurnal tides is computed in the
269 following way. First, at each spatial grid point, we take half the difference of two measurements
270 taken at local times roughly 12 hours apart. This eliminates the mean value, removes the

271 semidiurnal and stationary planetary wave signals, and leaves the diurnal variations (assuming
272 that higher order periodicities are negligible). It is important to note that GOLD affords
273 approximately 10-hour local time differences rather than the ideal 12-hour because of the SZA
274 restrictions. Because the same local times, longitudes, and latitudes are sampled each day, taking
275 multiple day averages of data can be done to smooth the variations due to short-term and long-
276 term traveling planetary waves. For dayside disk sampling from geostationary orbit, computing
277 ~12-hour local time differences is achieved by taking the difference of measurements near dusk
278 and dawn. We interpolate to the earliest morning local time and the latest evening local time
279 possible to take the maximum constant local time difference. Additionally, we require that the
280 SZA for the dusk and dawn data points are within 1 degree because offsets in SZA would
281 introduce large biases (Figure 1a). This requirement typically leads to data being analyzed at
282 SZA $\sim 70^\circ$.

283 The non-migrating diurnal proxy at each latitude bin is then specified by the deviations
284 from the zonal mean of the dusk – dawn differences. For each latitude, the method of analysis
285 proceeds by normalizing the longitudinal perturbations. For temperatures, this is done by
286 dividing by the maximum temperature perturbation M_T , i.e., the maximum deviation from the
287 zonal mean of the dusk – dawn differences. Similarly, for $\Sigma O/N_2$, this is done by dividing by the
288 maximum $\Sigma O/N_2$ perturbation M_R . In this way, temperature and $\Sigma O/N_2$ are weighted evenly in
289 the fit. The normalized longitudinal perturbations serve as the observations to be fitted to in a
290 least squares approach. When least squares fitting, we use Fourier harmonics which include
291 correction terms accounting for the less than 12-hour local time differences following Oberheide
292 et al. (2002). At a constant latitude and altitude, a tidal component with period n and zonal

293 wavenumber s induces a perturbation in universal time t and longitude λ of the form, following
 294 Zhang et al., (2006),

$$A_{n,s} \cos(n\Omega t + s\lambda - \phi_{n,s}) \quad (4)$$

295 Where $s < 0$ denotes eastward zonal propagation, Ω is the rotation rate of the Earth, $A_{n,s}$ is the
 296 tidal component's amplitude, and ϕ is the tidal component's phase (typically defined as the
 297 universal time of maximum at 0° longitude). It is commonplace to analyze spacecraft
 298 measurements in the local time frame. The conversion between local time t_{LT} and universal time
 299 t is the following:

$$t_{LT} = t + \lambda/\Omega \quad (5)$$

300 Substituting Eqn. 5 into Eqn. 4 yields the tidal perturbation in the local time frame:

$$A_{n,s} \cos(n\Omega t_{LT} + (s - n)\lambda - \phi_{n,s}) \quad (6)$$

301 Migrating tides ($n = s$) are thus longitudinally invariant at a constant local time while non-
 302 migrating ($n \neq s$) control longitudinal variability in the local time frame. The temperature non-
 303 migrating diurnal proxies at a single latitude, as a function of longitude λ , can be expressed by
 304 Eqn. 7 where T_1 and T_2 are expressions for tidal perturbations consisting of DE3 and DE2 at
 305 local times t_1 and t_2 , respectively (see Eqns. 8 and 9). Residual contributions due to tidal
 306 components not captured in the fitting, DO for example, contributes to the uncertainty in the
 307 estimated tidal parameters. In this analysis, t_1 denotes a morning local time, t_2 , an evening local
 308 time.

$$\Delta T(\lambda) = T_2(\lambda) - T_1(\lambda), \quad (7)$$

$$T_1(\lambda) = T_{DE3} \cos(\Omega t_1 - 4\lambda - \phi_{DE3}) + T_{DE2} \cos(\Omega t_1 - 3\lambda - \phi_{DE2}) + T_b, \quad (8)$$

$$T_2(\lambda) = T_{DE3} \cos(\Omega t_2 - 4\lambda - \phi_{DE3}) + T_{DE2} \cos(\Omega t_2 - 3\lambda - \phi_{DE2}) + T_b, \quad (9)$$

312 T_{DE3} and T_{DE2} denote the DE3 and DE2 temperature amplitudes, ϕ_{DE3} and ϕ_{DE2} , the DE3 and
313 DE2 temperature phases. Ω is the Earth's rotation rate. T_b denotes a tidal bias term which
314 vanishes in the local time difference. Eqn. 10 gives an analytical expression of the local time
315 difference if only DE3 and DE2 contribute to the non-migrating diurnal proxy. Note that $\Delta t =$
316 $t_2 - t_1 - 12$. Eqn. 11 is the corresponding expression for $\Sigma O/N_2$ where R_{DE3} and R_{DE2} denote
317 the DE3 and DE2 $\Sigma O/N_2$ amplitudes, Φ_{DE3} and Φ_{DE2} , the DE3 and DE2 $\Sigma O/N_2$ phases.

$$318 \quad \Delta T(\lambda) = 2T_{DE3} \cos\left(\Omega \frac{\Delta t}{2}\right) \cos\left(\Omega t_2 + \Omega \frac{\Delta t}{2} - 4\lambda - \phi_{DE3}\right) + 2T_{DE2} \cos\left(\Omega \frac{\Delta t}{2}\right) \cos\left(\Omega t_2 + \Omega \frac{\Delta t}{2} - 3\lambda - \phi_{DE2}\right), \quad (10)$$

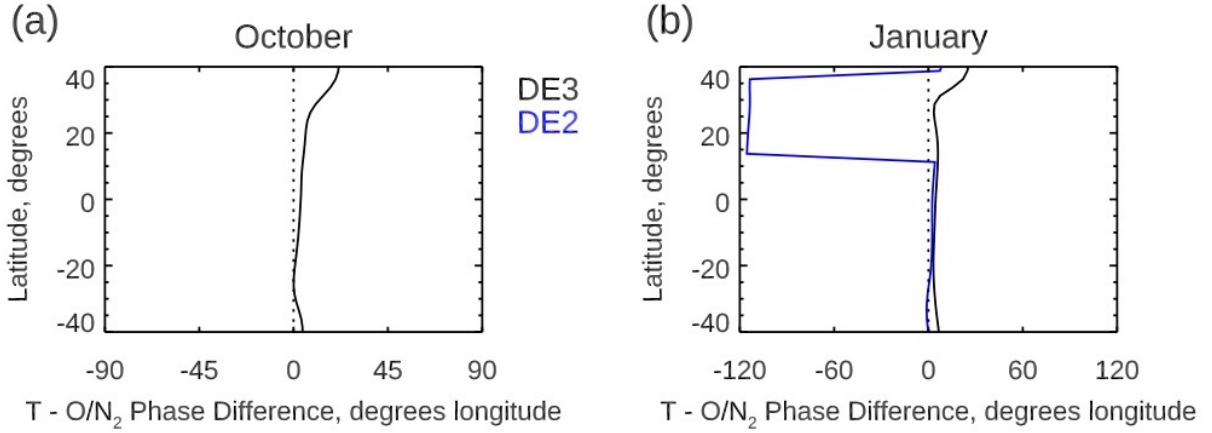
$$319 \quad \Delta R(\lambda) = 2R_{DE3} \cos\left(\Omega \frac{\Delta t}{2}\right) \cos\left(\Omega t_2 + \Omega \frac{\Delta t}{2} - 4\lambda - \Phi_{DE3}\right) + 2R_{DE2} \cos\left(\Omega \frac{\Delta t}{2}\right) \cos\left(\Omega t_2 + \Omega \frac{\Delta t}{2} - 3\lambda - \Phi_{DE2}\right), \quad (11)$$

320 The $\Sigma O/N_2$ phases Φ_{DE3} and Φ_{DE2} are constrained by the prescribed phase differences at the
321 latitude of interest (Eqns. 12 and 13).

$$322 \quad \Phi_{DE3} = \phi_{DE3} - \Theta_{DE3}, \quad (12)$$

$$323 \quad \Phi_{DE2} = \phi_{DE2} - \Theta_{DE2}, \quad (13)$$

324 Θ_{DE3} and Θ_{DE2} are the temperature – $\Sigma O/N_2$ phase differences for DE3 and DE2 respectively
325 (Figure 4). To best fit the data, the prescribed phase differences are allowed to vary +/- 10° of
326 longitude.



327

328 **Figure 4.** From TIE-GCM simulations, neutral temperature – $\Sigma O/N_2$ tidal phase difference as a
 329 function of latitude, in units of degrees of longitude of maximum at 0 LT, for October (a) and
 330 January (b). DE3 in black, DE2 in blue.

331

In Eqn. 11, the $\Sigma O/N_2$ amplitudes R_{DE3} and R_{DE2} are related to the temperature

332

amplitudes by factors k_1 and k_2 (Eqns. 14 and 15). The optimal values for k_1 and k_2 , when

333

applying our approach to the TIE-GCM dataset (Section 2.2), are respectively given by Eqns. 16

334

and 17, where T_{DE3}^{model} and T_{DE2}^{model} denote the DE3 and DE2 temperature amplitudes derived from

335

the fully sampled TIE-GCM dataset and R_{DE3}^{model} and R_{DE2}^{model} denote those for $\Sigma O/N_2$.

336

$$R_{DE3} = k_1 T_{DE3}, \quad (14)$$

337

$$R_{DE2} = k_2 T_{DE2}, \quad (15)$$

338

$$k_1 = \frac{R_{DE3}^{model}}{T_{DE3}^{model}} \frac{M_T}{M_R}, \quad (16)$$

339

$$k_2 = \frac{R_{DE2}^{model}}{T_{DE2}^{model}} \frac{M_T}{M_R}, \quad (17)$$

340

However, when applying our approach to the GOLD dataset (Section 4.2), we set $k_1 = 1$ and

341

$k_2 = 1$. This is done because the observed ratio of the maximum temperature perturbation (K)

342

to the maximum $\Sigma O/N_2$ perturbation (%) deviates from the modeled ratio by as much as 200%.

343 This large divergence is likely a consequence of differences between the observed and modeled
 344 atmospheres related to the tidal vertical winds and the rate of dissipation/nonlinearity in the tides.
 345 In October, we require that $T_{DE3} \geq 3T_{DE2}$ to ensure that DE3 is much higher in amplitude than
 346 DE2. This constraint is justified for this season because DE3 has consistently been identified as
 347 the dominant non-migrating diurnal component around September equinox on a climatological
 348 basis (Forbes et al., 2006; Nischal et al., 2019).

349 In order to deduce the tides, the normalized non-migrating diurnal proxies for
 350 temperature and $\Sigma\text{O}/\text{N}_2$, T_{obs} and R_{obs} , are simultaneously fitted to Eqns. 10 and 11. A least-
 351 squares scheme determines the combination of temperature tidal parameters T_{DE3} , T_{DE2} , ϕ_{DE3} ,
 352 and ϕ_{DE2} that yields the lowest total squared residual $T_{res}^2 + R_{res}^2$ (Eqn. 18).

$$353 \quad T_{res}^2 + R_{res}^2 = [T_{obs}(\lambda) - \Delta T(\lambda)]^2 + [R_{obs}(\lambda) - \Delta R(\lambda)]^2, \quad (18)$$

354 We have implemented a pattern search optimization approach (Lewis et al., 2000) to efficiently
 355 determine a solution. The five best combinations of tidal parameters are determined from a 25
 356 $\times 25 \times 25$ parameter grid and serve as initial guesses. For each initial guess, the residual
 357 value is then compared to those at each of its neighboring grid points after the parameter grid
 358 resolution is halved. If one of the neighboring grid points yields a lower total squared residual,
 359 then the center moves to that point. If the center is the best guess, then the parameter grid
 360 resolution is further halved. This process proceeds until there have been 4 reductions. The
 361 deduced tidal parameters are taken from best result out of the five pattern searches starting from
 362 the initial guesses. The retrieved temperature and $\Sigma\text{O}/\text{N}_2$ amplitudes in normalized units are
 363 then converted back to geophysical units by multiplying by the respective maximum
 364 perturbation, i.e., M_T and M_R .

365

366 4) Results

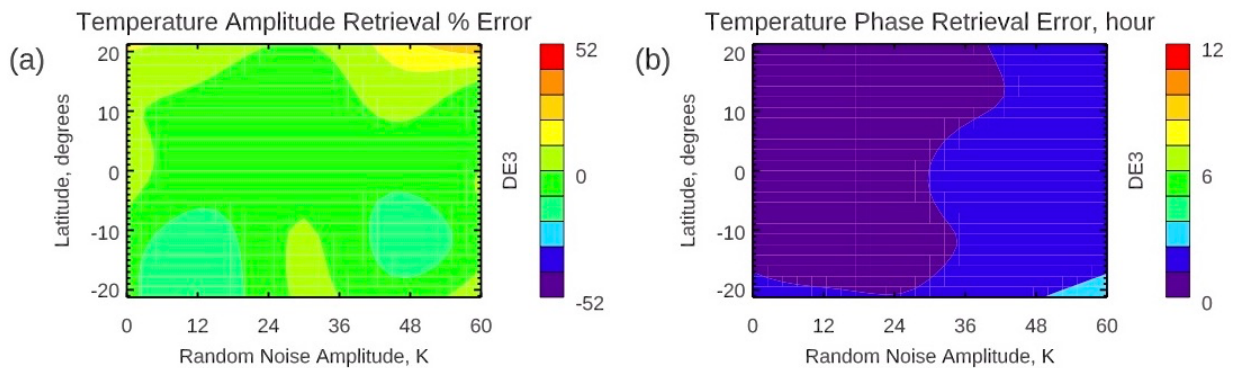
367 4.1 TIE-GCM Sensitivity Analyses

368 Testing our approach on the TIE-GCM-simulated GOLD dataset, consisting of the
369 effective neutral temperature and vertical column density ratio of O to N₂ (described in Section
370 2), allows us to examine its reliability when applied to a dataset in which the true tides are
371 known. This dataset contains a realistic tidal spectrum and is sampled in the observational
372 geometry of GOLD. Two test cases are considered: October and January during solar minimum
373 conditions. For both, we deduce DE3 and DE2 between -21.25° to 21.25° latitude. We restrict
374 our analysis to this latitude range as it is where DE3 and DE2 have their largest amplitudes
375 (Figures 2 and 3). Robustness of our algorithm to noise is tested using runs at 5 linearly
376 increasing levels of random noise where the maximum noise magnitude for temperature is 60
377 Kelvins and 0.08 (~15%) for $\Sigma\text{O}/\text{N}_2$. We performed 10 simulations at each noise level and
378 compare the average result to the truth to reduce random effects in the amplitude and phase
379 errors.

380 During October, DE3 is the most dominant non-migrating tide (Figure 2). Shown in
381 Figure 5a is the percent error in the temperature amplitude retrieval for DE3 as a function of
382 latitude and random noise magnitude. Figure 5b shows the absolute error (in units of hours of
383 universal time) of the phase retrieval for DE3. The $\Sigma\text{O}/\text{N}_2$ results are similar and are thus not
384 shown. The errors in the deduced DE2 tide are not shown because the DE2 amplitude is small
385 during October. The DE3 phases (Figure 5b) are retrieved very accurately even in the case of
386 maximum random noise. The error in the deduced DE3 amplitude (Figure 5a) strongly depends
387 on random noise amplitude and latitude. For the lowest noise amplitudes, the error is negligible.

388 For the case of maximum noise amplitude, the DE3 temperature amplitude is overestimated by
389 about 40% at 21.25° N, but elsewhere the error is negligible.

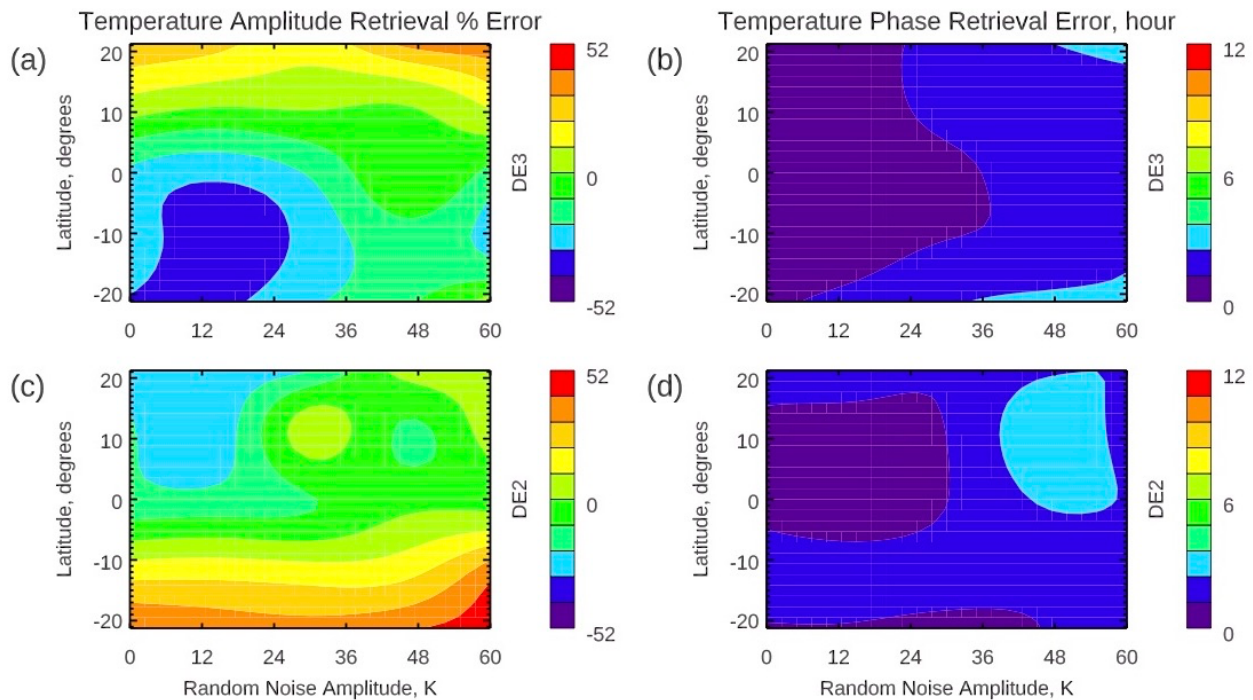
390 To assess the assumption that only two tides are present, we applied our approach to a
391 modified dataset where we remove the terdiurnal tide and all components in the non-migrating
392 diurnal spectrum except for DE3 and DE2. This filtering removes the tidal aliasing caused by
393 components assumed to be zero and removes any bias in the zonal mean caused by a partially
394 viewed component such as DO, for example. It was found that the errors in deduced tidal
395 parameters do not change appreciably (supplementary material, Figure S1). This suggests that
396 tidal aliasing does not play a major role and that the errors present in Figure 5 are primarily due
397 to random noise and the restriction in longitude.



398
399 **Figure 5.** Retrieval errors as a function of latitude and random noise amplitude for DE3
400 temperature tidal amplitudes (a) and phases (b) when applying our approach to a simulated
401 GOLD dataset for October and solar minimum conditions.

402 Figure 6 is the same as Figure 5 but for January. The errors in the deduced DE2 are
403 included since, along with DE3, it is the leading non-migrating diurnal tide (Figure 3). Figures
404 6a and 6c show the percent error in the deduced temperature amplitude for DE3 and DE2
405 respectively. The DE3 amplitude is underestimated by ~40% in the southern hemisphere at the

406 second noise level (12 K) while DE2 is overestimated by as much as ~50% for the highest noise
 407 level (60 K). Interestingly, the underestimation of the DE3 amplitude in the southern hemisphere
 408 is smaller for the highest noise levels. A possible explanation is that the random noise drowns
 409 out the residual contributions from other non-migrating diurnal tides. Phase retrieval error as
 410 shown by Figures 6b and 6d is negligible for both DE3 and DE2, always less than 4 hours. As
 411 was done for October, we applied our approach to a modified dataset where only DE3 and DE2
 412 remain. It was found that the errors in the retrieved tidal amplitudes are smaller when residual
 413 contributions from other components are removed (supplementary material, Figure S2).
 414 Therefore, more so than in October conditions, aliasing of tides assumed to be absent contributes
 415 to uncertainty in the retrieved amplitudes.



416

417

418 **Figure 6.** Same as Figure 5, but for January and the errors in the retrieved DE2 tidal

419 parameters are also shown.

420 4.2 Application to the GOLD Dataset

421 In this subsection we discuss application of our approach (discussed in Section 3) to
422 GOLD observations from two weeks during different seasons: 21-27 October 2018 and 8-14
423 January 2020. These fitting periods were selected to be (1) long enough to smooth large day-to-
424 day tidal variability (Li et al., 2015; Pedetalla et al., 2016), (2) representative of times when non-
425 migrating tides are strong and somewhat different, and (3) absent of rapid changes, e.g., during a
426 sudden stratospheric warming or geomagnetic storm. Our analysis is conducted between -25° to
427 25° latitude. We initially analyze the data in the irregularly spaced latitude-longitude spatial grid
428 provided in the GOLD data products. While this would not be justified at mid to high latitudes,
429 there is only a negligible change in latitude across a row of pixels reported on the disk within this
430 latitude range. The value at each disk pixel (longitude, latitude) and scan (universal time) in our
431 analysis represents the 7-day mean. About 68 GOLD dayside disk scans are performed at about
432 the same universal times each day during the respective time periods. It is assumed that the tidal
433 amplitudes and phases are time-invariant during the fitting period. GOLD disk neutral
434 temperature responds episodically to variations in geomagnetic and solar activity (not shown)
435 while $\Sigma\text{O}/\text{N}_2$ exhibits response to geomagnetic activity (Cai et al., 2020). Therefore, we ensure
436 that only days with sufficiently low geomagnetic and solar activity are used in the analysis. Our
437 geomagnetic activity threshold is $K_p > 4$ and our solar activity threshold is a F10.7cm index
438 more than 2.5 standard deviations higher than the mean F10.7cm index over a window equal to
439 the fitting period ± 7 days. Data are also treated for outliers by removing data points for a
440 given pixel/scan that are 2 standard deviations from the median value (most 7-day time series for
441 a pixel/scan contain one outlier, if any). Also, we disregard the edge rows of pixels around the
442 equator where data quality may be lower (due to reduced sensitivity of the detector near the end

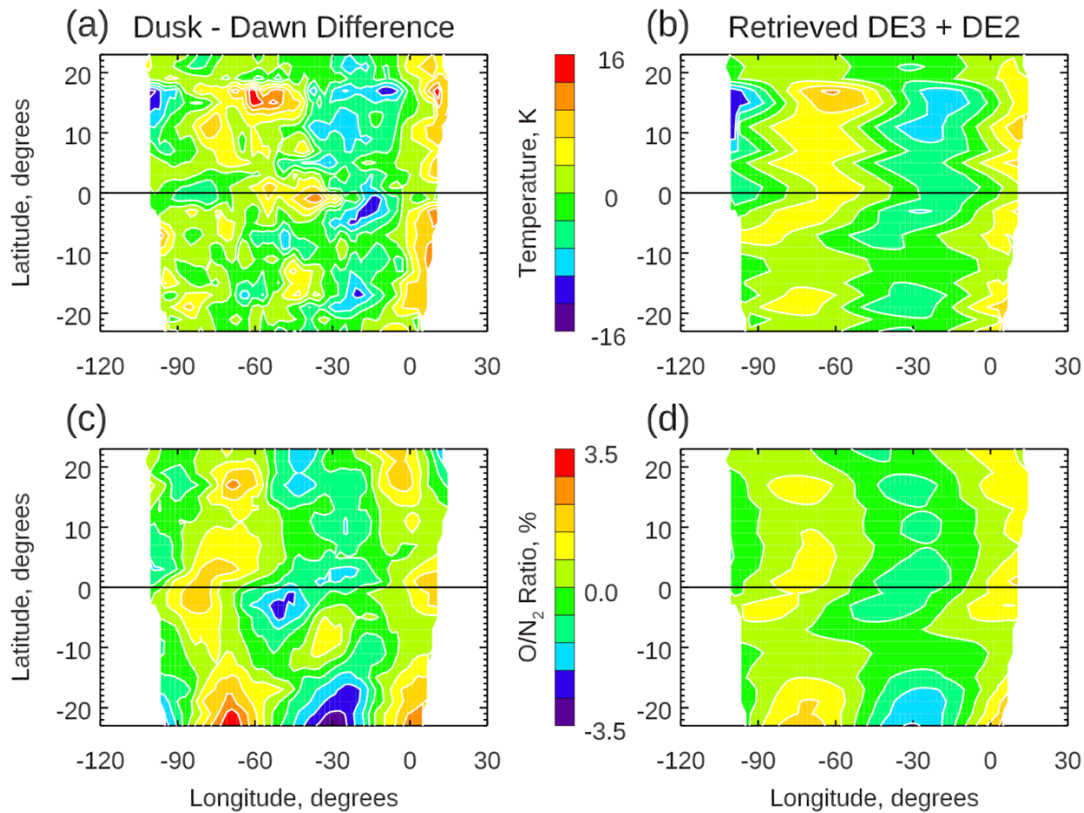
443 of the entrance slit). The standard deviation for the 7-day means corresponding to a given
444 pixel/scan is on average about 50 K for temperature and 6% relative to the zonal mean for $\Sigma\text{O}/\text{N}_2$
445 at the latitudes/SZA analyzed. Additionally, we found it necessary to remove linear trends with
446 longitude from the non-migrating diurnal proxies (especially $\Sigma\text{O}/\text{N}_2$) at some latitudes. This
447 linear detrending makes the salient wave signal more apparent. One may consider that the linear
448 trends with longitude are the actual tides (which must have zonal wavelengths larger than the
449 GOLD field-of-regard, i.e., zonal wavenumber 1 or 2), and the residuals reflect random noise.
450 But this is unlikely since analysis of slightly offset fitting periods or the same season in different
451 years yields similar $\Sigma\text{O}/\text{N}_2$ morphology after the linear trends are removed (not shown). Before
452 performing the least squares fit to the tidal perturbation equations, we interpolate the normalized
453 longitudinal perturbations to an evenly spaced longitude grid so that each sector of longitude is
454 equally weighted in the fit. The non-migrating diurnal proxies are also smoothed in the
455 longitude dimension. We estimate the resultant damping of the dominant tidal amplitudes(s) is
456 on the order of 5%. In what follows, we present results for each time period.

457 Both TIE-GCM simulations (see Figure 2) and SABER observations of MLT temperature
458 (Forbes et al, 2006) indicate that DE3 is the dominant tidal component at/around September
459 equinox. DE2 is the secondary tide in our analysis during this time because of its similar modal
460 structure to that of DE3. In Figure 7, we compare global maps of the dusk – dawn difference
461 (non-migrating diurnal proxy) and the retrieved tides (DE3 + DE2) for temperature (K) and
462 $\Sigma\text{O}/\text{N}_2$ (% relative to the zonal mean at each latitude). Figures 7a and Figure 7b respectively
463 indicate peak-to-peak perturbations of about 32 K and 7%. The latitudinal structure is not
464 symmetric, and the phase rapidly changes with latitude especially in temperature. It is
465 noteworthy that both the temperature and the $\Sigma\text{O}/\text{N}_2$ dusk and dawn differences exhibit these

466 features. This similarity may be explained by a combination of (1) similar tidal dynamics and
467 (2) instrument or processing artifacts. It is not surprising that the northern hemisphere and
468 southern hemisphere are not coherent since there are clear hemispheric biases in the GOLD disk
469 neutral temperature and $\Sigma\text{O}/\text{N}_2$ measurements (not shown) caused by varying instrument
470 characteristics along the slit that are not currently removed in the processing of FUV radiances
471 (McClintock et al., 2020b). Additionally, the relatively high uncertainty in the retrieved disk
472 neutral temperature at high SZA analyzed leads to the noisy dusk – dawn differences in Figure
473 7a, perhaps best exemplified by the unphysical change in temperature north of (60° W, 15° N).

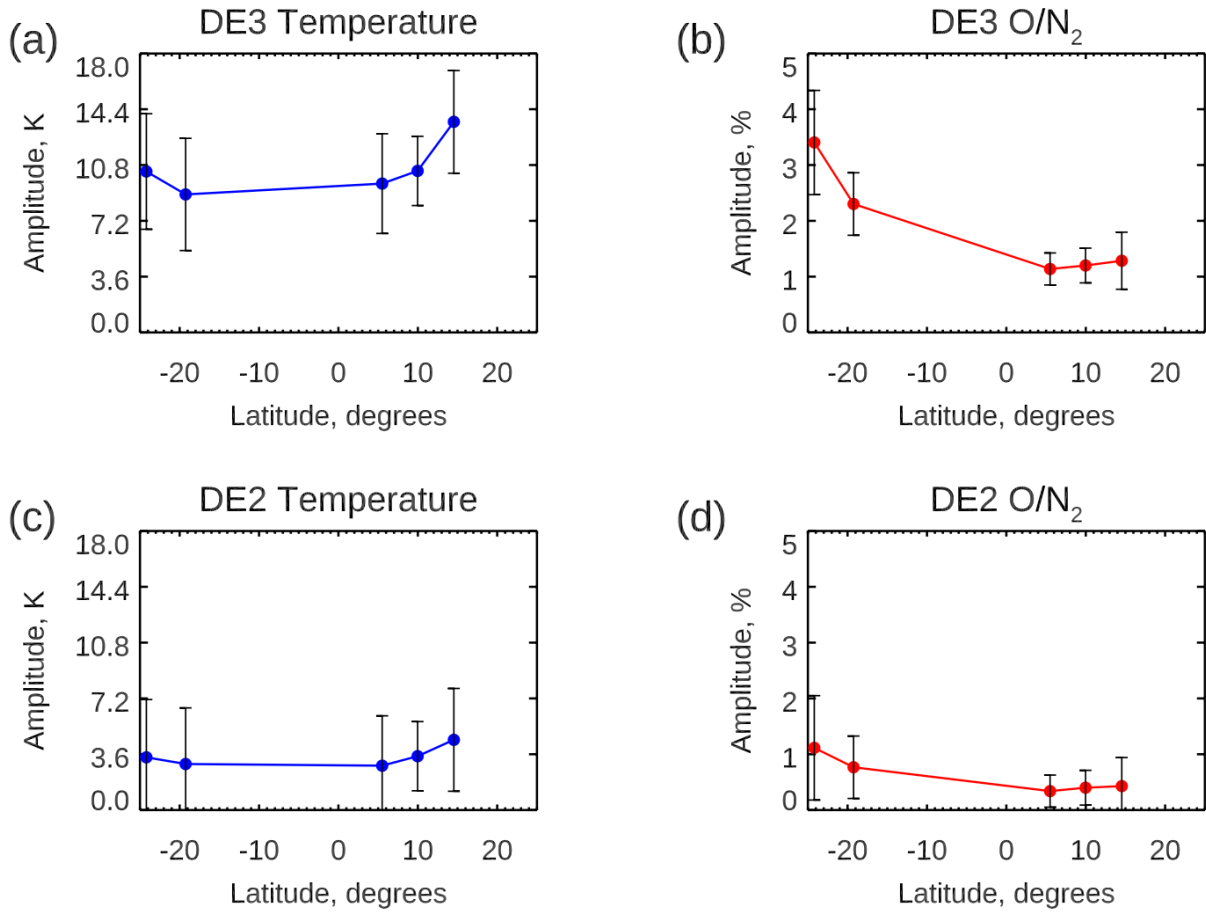
474 Figures 8 and 9 respectively show the retrieved amplitudes and phases as functions of
475 latitude. We show select latitudes where the correlation coefficient between the non-migrating
476 diurnal proxy and retrieved tides is greater than 0.75 for both temperature and $\Sigma\text{O}/\text{N}_2$. The error
477 bars represent the root mean square deviation of the least squares fit at each latitude and indicate
478 the degree of uncertainty. Figure 8a shows that the DE3 temperature amplitude is mostly above
479 10 K which is greater than that from TIE-GCM (Figure 2a). The DE3 $\Sigma\text{O}/\text{N}_2$ amplitudes shown
480 in Figure 8b are markedly higher in the southern hemisphere than in the northern hemisphere.
481 The amplitude in the southern hemisphere is greater than that from TIE-GCM (Figure 2b).
482 Results for DE2 amplitudes (Figures 8c and 8d) are similar but much lower in amplitude. The
483 results in Figure 8 indicate the DE3 and DE2 amplitudes required to generate the perturbations in
484 Figures 7a and 7b and provide the first estimates of non-migrating diurnal tidal amplitudes in
485 middle thermosphere temperature. Phases as a function of latitude are shown in Figure 9 in units
486 of universal time of maximum at 0° longitude. All the retrieved phases for a given component
487 and parameter appear to be within about 4 hours. This suggests that we are seeing the same
488 wave at these latitudes while the tides at other latitudes are perhaps obscured by instrument

489 artifacts or limitations associated with using GOLD disk neutral temperature at high SZA. In
490 general, the retrieved tides generally reproduce the large-scale morphology of the dusk – dawn
491 differences (compare Figure 7a to 7b and 7c to 7d). It does not do so when the phase difference
492 between the temperature and $\Sigma O/N_2$ variations differs much more than 10° longitude from the
493 prescribed phase difference provided by TIE-GCM. Proving what causes this discrepancy is
494 beyond the scope of this work but they may differ because of (1) instrument/algorithm artifacts
495 present in the GOLD data or (2) TIE-GCM does not perfectly represent the real atmosphere.



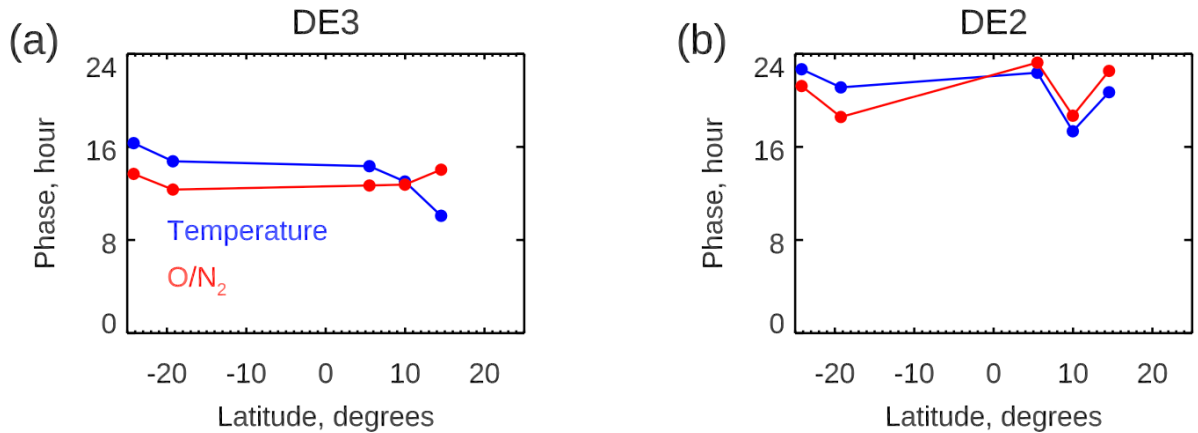
496
497 **Figure 7.** Global maps of the dusk – dawn differences and retrieved tides DE3 + DE2 in neutral
498 temperature, (a) and (b), and column O/N₂ ratio, (c) and (d), from GOLD data in October 2018.

499



500
501
502
503
504
505
506

Figure 8. Retrieved amplitudes from GOLD data during October 2018 as a function of latitude for DE3, (a) and (b), and DE2, (c) and (d). Errors bars reflect the root mean square deviation of the least squares fit at each latitude. Only latitudes where the least squares fit in both temperature and O/N₂ yields a correlation coefficient greater than 0.75 are shown.

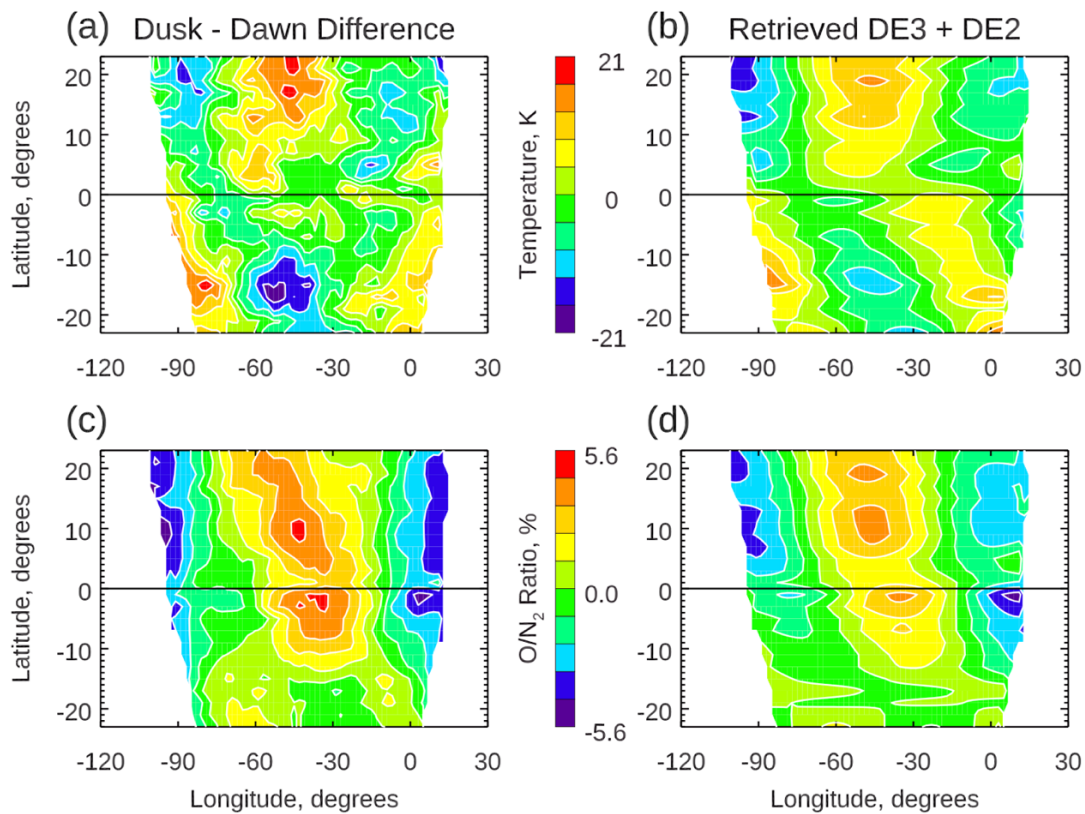


507

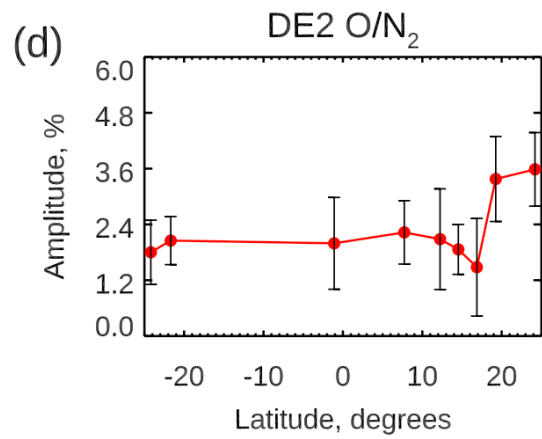
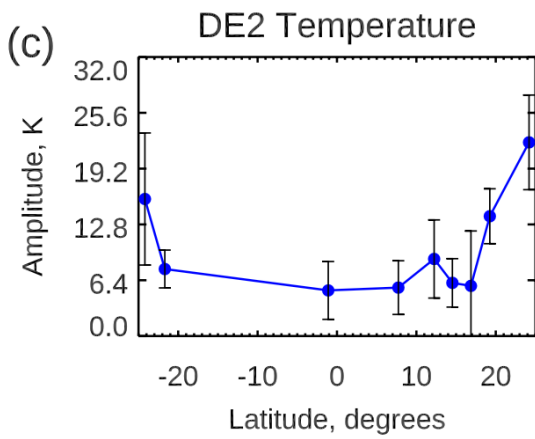
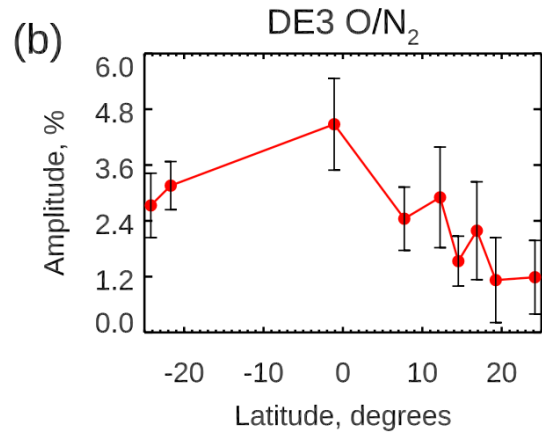
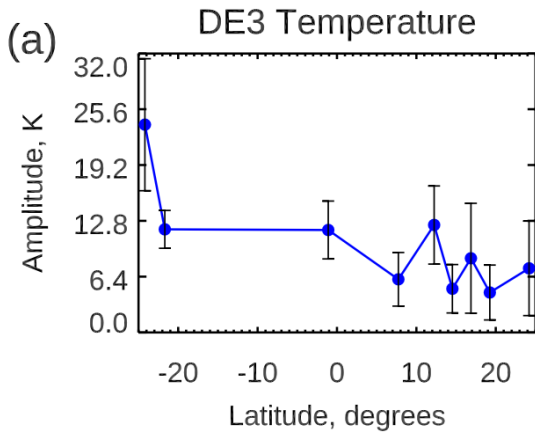
508 **Figure 9.** Retrieved phases (universal time of maximum at 0° longitude) from GOLD data
 509 during October 2018 as a function of latitude for DE3 (a) and DE2 (b). Temperature is shown
 510 in blue, O/N₂ in red. Only latitudes where the least squares fit in both temperature and O/N₂
 511 yields a correlation coefficient greater than 0.75 are shown.

512 TIE-GCM (Figure 3) indicates that DE3 and DE2 are the leading components in the non-
 513 migrating diurnal spectrum around January solstice. Forbes et al. (2008) analyzed
 514 TIMED/SABER temperatures from 2003-2005 and showed that DE2 was the dominant non-
 515 migrating diurnal tide at the equator and at 116 km altitude around January solstice, with DE3
 516 being minor. Informed by both modeling and observations, we deduce DE3 and DE2 during
 517 January 2020. Figures 10, 11, and 12 are the same as Figures 7, 8, and 9 but when we apply our
 518 approach to GOLD data analyzed over 8-14 January 2020. The dusk – dawn differences
 519 (Figures 10a and 10c) respectively have peak-to-peak perturbations of about 42 K and about
 520 11%. Figure 10b and 10d reproduce the large-scale structure present in Figures 10a and 10c
 521 respectively. Figure 10a, like its October counterpart (Figure 7a), exhibits seemingly random
 522 fluctuations as well as a lack of latitude symmetry. The same reasons discussed above for
 523 October 2018 likely explain these features. Figure 10c shows that for Σ O/N₂ there is a coherent
 524 structure in the non-migrating diurnal tide with zonal wavelength approximately equal to 100° of

525 longitude between -10° S and 25° N. This suggests that a superposition of DE3 and DE2 are
 526 responsible for generating the signature. Figures 11a and 11b indicate that both the DE3 and
 527 DE2 temperature amplitudes are on the order of 10 K barring the outlier results at -25° S and -25°
 528 N which have large error bars. Figure 11b shows that the DE3 $\Sigma O/N_2$ amplitude is highest
 529 around the equator ($\sim 4.8\%$), while Figure 11d shows DE2 $\Sigma O/N_2$ amplitude is highest in the
 530 northern hemisphere. The DE2 phases (Figure 12b) deviate no more than about 4 hours from
 531 0:00 except at -1° S, while the DE3 phases vary more with latitude. This suggests that the DE3
 532 retrieval is perhaps more impacted by instrument artifacts and limitations associated with using
 533 GOLD disk neutral temperature at high SZA while the DE2 seen is a single coherent wave.



534
 535 **Figure 10.** Same as Figure 7 but for 8-14 January 2020.



536

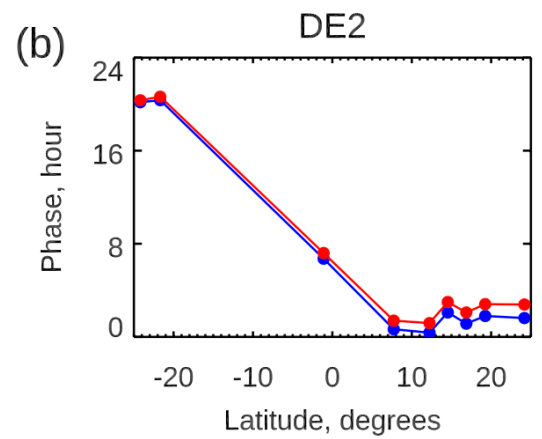
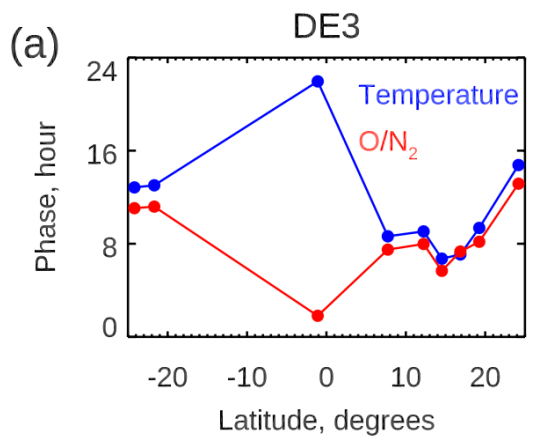
537 **Figure 11.** Same as Figure 8 but for 8-14 January 2020.

538

539

540

541



542

543 **Figure 12.** Same as Figure 9 but for 8-14 January 2020.

544 **5) Summary and Conclusions**

545 We have presented a synoptic view of non-migrating diurnal tides in the middle
546 thermosphere temperature and composition using GOLD, the first of its kind from an
547 observational platform in geostationary orbit. To accomplish this, we have employed a novel
548 approach to estimate non-migrating diurnal tides in the middle thermosphere. Our approach
549 derives two specified non-migrating tides, i.e., DE3 and DE2, from simultaneous observations of
550 temperature and composition ($\Sigma\text{O}/\text{N}_2$) by taking dusk – dawn differences, while constraining
551 temperature – composition phase relationships using TIE-GCM. We have provided the first
552 estimates of non-migrating diurnal tidal amplitudes in middle thermosphere temperature. The
553 DE3 and DE2 amplitudes required to explain the observed diurnal variations exceed the
554 respective TIE-GCM amplitudes. The latitudinal structure of the retrieved tides exhibit a lack of
555 continuity and symmetry, not present in TIE-GCM simulations, possibly caused by a
556 combination of (1) unrepresented tidal dynamics, (2) relatively high uncertainty of GOLD disk
557 neutral temperature at higher SZA, and (3) instrument/algorithm artifacts. Nevertheless, even
558 estimates with $\sim 50\%$ amplitude retrieval errors provide much needed constraints on temperature
559 tides in the middle thermosphere. A systematic removal of contaminant ionospheric contribution
560 to the observed $\Sigma\text{O}/\text{N}_2$ tides will be the topic of a future work.

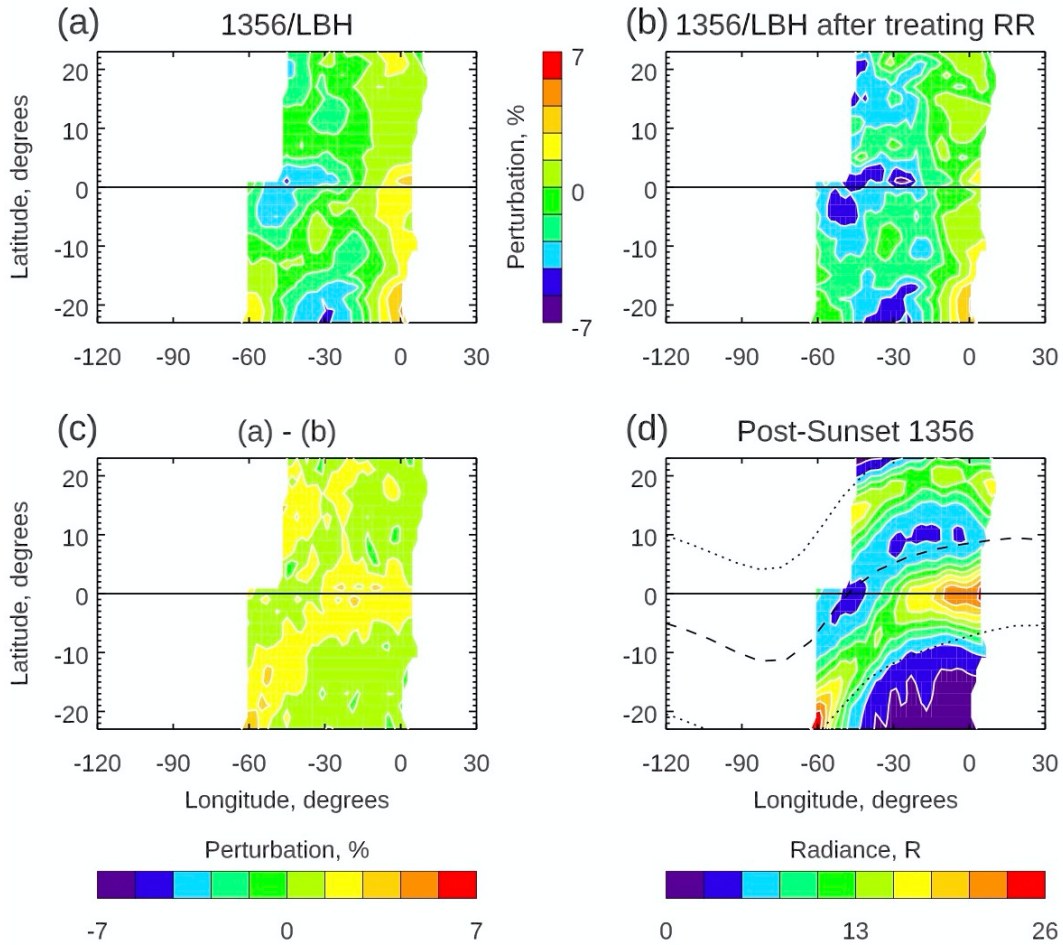
561

562 **Appendix: Assessing the Impact of Ionospheric Contamination**

563 O^+ radiative recombination by the equatorial arcs has the potential to impact the global
564 structure of the $\Sigma\text{O}/\text{N}_2$ dusk – dawn differences. Previous studies (e.g., Kil et al., (2013) and
565 references therein) have shown that investigations of non-migrating tides in $\Sigma\text{O}/\text{N}_2$ retrieved
566 from far ultraviolet dayglow are impacted by O^+ radiative recombination in the ionosphere,

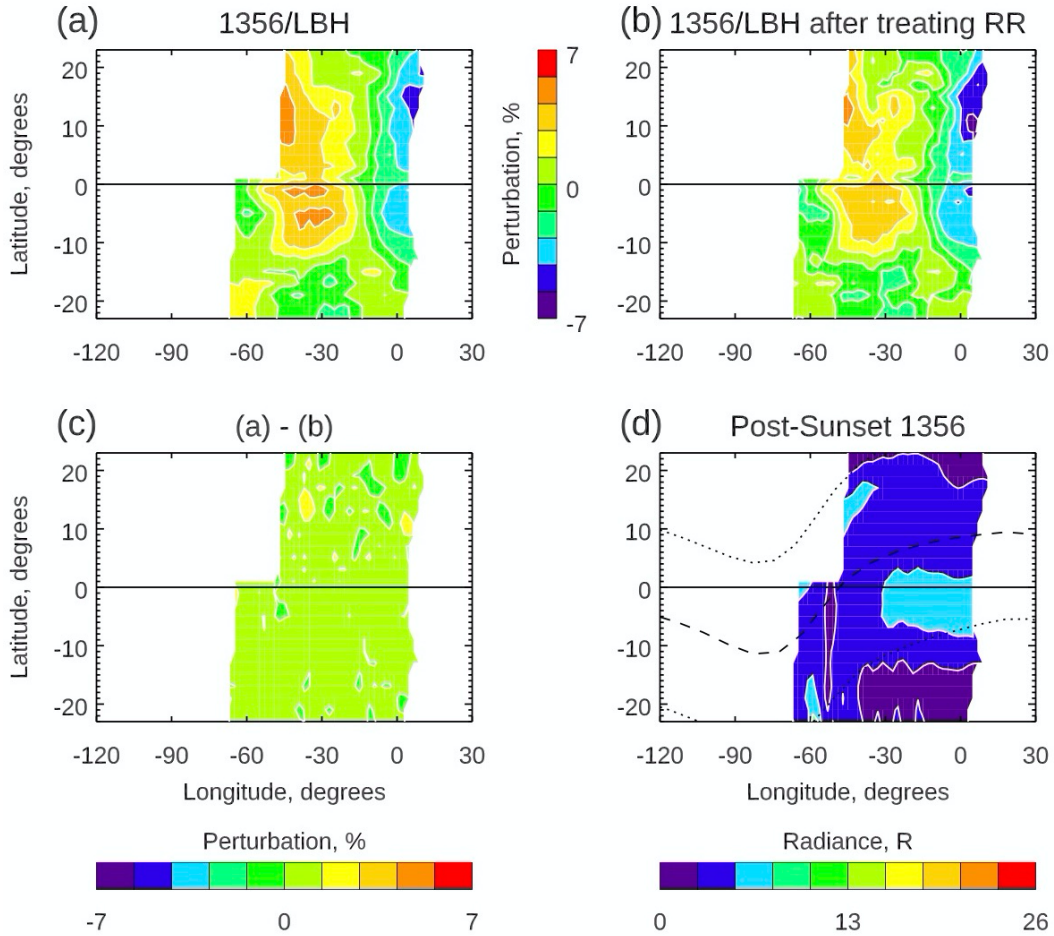
567 concentrated around the equatorial ionization anomaly (EIA), which emits at the same
568 wavelength, 135.6 nm, used in the $\Sigma O/N_2$ retrieval. Kil et al. (2013) concluded that the
569 longitudinal wave patterns in GUVI $\Sigma O/N_2$ near 15:00 LT mostly reflect the ionosphere 135.6
570 nm emissions. The tidal variations in the O^+ radiative recombination likely correlate with those
571 in F-region plasma density which are driven by E-region dynamo modulation by tidal winds
572 (England et al., 2006; Immel et al., 2006). In general, the $\Sigma O/N_2$ tidal signatures near the EIA
573 may be produced by a superposition of the thermospheric tides and the ionospheric
574 contamination, which should both have the same wavenumber structure but are out of phase. It
575 is expected that $\Sigma O/N_2$ near the morning terminator is less impacted by the ionosphere (since
576 nighttime recombination depresses the O^+ density). In the following, we assess the potential
577 impact of ionospheric contamination on the $\Sigma O/N_2$ non-migrating diurnal proxies used in our
578 approach. GOLD has the unique advantage of measuring post-sunset 135.6 nm emissions of the
579 ionosphere in the same sector of the Earth over which $\Sigma O/N_2$ is retrieved during daytime (Eastes
580 et al., 2019). We use version 04 GOLD night scans, exclusively channel B, to construct a map of
581 post-sunset 135.6 nm emissions by averaging into a local time bin extending from 19:00-22:00
582 LT. These maps serve as a proxy for the ionospheric contribution to 135.6 nm emissions around
583 dusk used in the $\Sigma O/N_2$ retrieval. The maps are constructed using data from 21-27 October 2018
584 and 8-14 January 2020. When analyzed in the same fashion, the dusk – dawn difference of the
585 ratio of the 135.6 nm and LBH band (1356/LBH) intensities correlate extremely well (not
586 shown) with those of $\Sigma O/N_2$ (shown in Figures 7c and 10c) since $\Sigma O/N_2$ is derived from
587 1356/LBH. We can therefore assess the potential impact of ionospheric contamination on our
588 approach by first removing the post-sunset 135.6 nm emissions from the dusk 135.6 nm
589 emissions used in the retrieval of $\Sigma O/N_2$ and then recomputing the 1356/LBH ratio. Figures 13a

590 and 13b compare 1356/LBH brightness ratios before and after the post-sunset 135.6 nm
591 emissions are removed for the period during October 2018. Note that there is a gap of
592 longitudinal coverage on the western side of the disk because GOLD does not perform night
593 scans in the entire region over which GOLD performs day scans. Figure 13c shows the
594 difference of the 1356/LBH before and after treating for ionospheric contamination. This
595 difference resembles the map of post-sunset 135.6 (Figure 13d) used in the removal. The
596 geomagnetic equator is indicated as a dashed line in Figure 13d, and the brightest post-sunset
597 135.6 nm emissions clearly follow the equatorial arcs and exhibit longitudinal asymmetry,
598 especially in the southern hemisphere. Figure 13c suggests that while the ionospheric
599 contamination appreciably affects the longitudinal asymmetry, it is not the dominant mode of
600 variability in the global structure of the 1356/LBH pattern. Therefore, ionospheric
601 contamination does not affect the zonal wavenumber or phase and likely thus does not
602 fundamentally change the retrieved tides. Figure 14 is the same as Figure 13 but for January
603 2020. The post-sunset 135.6 nm emissions (Figure 14d) are dimmer during this time and the
604 resulting difference between the 1356/LBH brightness ratios before and after treating
605 ionospheric contamination (Figure 14c) is smaller. It is evident that ionospheric contamination
606 has a seasonal dependence such that our results in October 2018 are more likely to be impacted
607 by ionospheric contamination. Although beyond the scope of the current work, it is conceivable
608 to produce a revised GOLD $\Sigma\text{O}/\text{N}_2$ product where the post-sunset 135.6 nm emissions are
609 removed from the retrieval input near dusk. From the above analysis, we expect the ionospheric
610 signature in GOLD $\Sigma\text{O}/\text{N}_2$ non-migrating tides to be minimal due to the pronounced dip in the
611 magnetic equator with respect to the geographic equator across the Earth in GOLD's field-of-
612 regard which would tend to smooth out any ionospheric signature in the non-migrating tides.



613
 614
 615
 616
 617
 618
 619
 620
 621

Figure 13. Dusk-dawn differences of 1356/LBH intensity ratios before (a) and after (b) O+ RR is removed from the dusk 1356 radiances. Presented as perturbations from the zonal mean of the 1356/LBH ratio. (c) shows the difference of (a) and (b). The global map (d) of post-sunset 1356 used in the O+ RR treatment. The dashed line indicates the geomagnetic equator. The dotted lines north and south of the geomagnetic equator indicate lines of constant geomagnetic latitude at +/- 15°.



622
623

624 **Figure 14.** Same as Figure 13 but for 8-14 January 2020.

625

626 Data Availability Statement

627 GOLD data are available from the GOLD Science Data Center

628 (<http://gold.cs.ucf.edu/search/>) and the NASA Space Physics Data Facility

629 (<https://spdf.gsfc.nasa.gov>). The TIE-GCM tidal parameters and contribution function used in

630 this work are available for peer-review purposes at

631 <https://figshare.com/s/1e29f99114a466f4dc08?file=27913752> (this will later be moved to the

632 Virginia Tech Library permanent repository and assigned a DOI).

633

634 **Acknowledgements**

635 This research was supported by NASA contract 80GSFC18C0061. The authors would
636 like to thank J. Correira (Computational Physics, Inc.) for reprocessing GOLD ON2 files used in
637 the preparation of this work.

638

639 **References**

640 Brownscombe, J. L., Nash, J., Vaughan, G., and Rogers, C. F. (1985), Solar tides in the middle
641 atmosphere. I: Description of satellite observations and comparison with theoretical calculations
642 at equinox, *Q. J. R. Meteorol. Soc.*, 111, 677-689. <https://doi.org/10.1002/qj.49711146902>.

643

644 Cai, X., Burns, A. G., Wang, W., Qian, L., Solomon, S. C., Eastes, R. W., et al. (2020). The two-
645 dimensional evolution of thermospheric $\Sigma\text{O}/\text{N}_2$ response to weak geomagnetic activity during
646 solar minimum observed by GOLD. *Geophysical Research Letters*, 47, e2020GL088838.
647 <https://doi.org/10.1029/2020GL088838>.

648

649 Cai, X., Burns, A. G., Wang, W., Qian, L., Solomon, S. C., Eastes, R. W., et al.
650 (2021). Investigation of a neutral ‘tongue’ observed by GOLD during the geomagnetic storm on
651 May 11, 2019. *Journal of Geophysical Research: Space Physics*, 126,
652 e2020JA028817. <https://doi.org/10.1029/2020JA028817>.

653

654 Chang, L. C., C.-H. Lin, J.-Y. Liu, N. Balan, J. Yue, and J.-T. Lin (2013), Seasonal and local
655 time variation of ionospheric migrating tides in 2007–2011 FORMOSAT-3/COSMIC and TIE-
656 GCM total electron content, *J. Geophys. Res. Space Physics*, 118, 2545–2564,
657 doi:10.1002/jgra.50268.

658

659 Correira, J., Evans, J. S., Krywonos, A., Lumpe, J. D., Veibell, V., McClintock, W. E., & Eastes,
660 R. W. (2020). Thermospheric composition and solar EUV flux from the Global-scale
661 Observations of the Limb and Disk (GOLD) mission. *Earth and Space Science Open Archive*,
662 36. <https://doi.org/10.1002/essoar.10501920.1>.

663

664 Cui, J., R. V. Yelle, T. Li, D. S. Snowden, and I. C. F. Müller-Wodarg (2014), Density waves in
665 Titan's upper atmosphere, *J. Geophys. Res. Space Physics*, 119, 490–518,
666 doi:10.1002/2013JA019113.

667

668 Eastes, R. W., McClintock, W. E., Burns, A. G., Anderson, D. N., Andersson, L., Aryal, S., et al.
669 (2020). Initial observations by the GOLD mission. *Journal of Geophysical Research: Space*
670 *Physics*, 125, e2020JA027823. <https://doi.org/10.1029/2020JA027823>.

671

672 Eastes, R. W., McClintock, W. E., Burns, A. G., Anderson, D. N., Andersson, L., Codrescu, M.,
673 et al. (2017). The Global-Scale Observations of the Limb and Disk (GOLD) Mission. *Space*
674 *Science Reviews*, 212(1-2), 383–408. <https://doi.org/10.1007/s11214-017-0392-2>.

675

676 Eastes, R. W., Solomon, S. C., Daniell, R. E., Anderson, D. N., Burns, A. G., England, S. L., et
677 al. (2019). Global-scale observations of the equatorial ionization anomaly. *Geophysical Research*
678 *Letters*, 46, 9318–9326. <https://doi.org/10.1029/2019GL084199>.

679

680 England, S. L. (2012), A review of the effects of non-migrating atmospheric tides on the Earth's
681 low-latitude ionosphere, *Space Sci. Rev.*, 168, 211–236, doi:10.1007/s112140119842-4.

682

683 England, S. L., Immel, T. J., Huba, D., Hagan, M. E., Maute, A., & DeMajistre, R. (2010).
684 Modeling of multiple effects of atmospheric tides on the ionosphere: An examination of possible
685 coupling mechanisms responsible for the longitudinal structure of the equatorial ionosphere.
686 *Journal of Geophysical Research*, 115, A05308. <https://doi.org/10.1029/2009JA014894>.

687

688 England, S. L., S. Maus, T. J. Immel, and S. B. Mende (2006), Longitudinal variation of the E-
689 region electric fields caused by atmospheric tides, *Geophys. Res. Lett.*, 33, L21105,
690 doi:10.1029/2006GL027465.

691

692 Forbes, J. M., J. Russell, S. Miyahara, X. Zhang, S. Palo, M. Mlynczak, C. J. Mertens, and M. E.
693 Hagan (2006), Troposphere-thermosphere tidal coupling as measured by the SABER instrument
694 on TIMED during July–September 2002, *J. Geophys. Res.*, 111, A10S06,
695 doi:10.1029/2005JA011492.

696

697 Forbes, J. M., X. Zhang, S. Palo, J. Russell, C. J. Mertens, and M. Mlynczak (2008), Tidal
698 variability in the ionospheric dynamo region, *J. Geophys. Res.*, 113, A02310,
699 doi:10.1029/2007JA012737.
700

701 Forbes, J. M., X. Zhang, E. R. Talaat, and W. Ward (2003), Nonmigrating diurnal tides in the
702 thermosphere, *J. Geophys. Res.*, 108(A1), 1033, doi:10.1029/2002JA009262.
703

704 García-Comas, M., F. González-Galindo, B. Funke, A. Gardini, A. Jurado-Navarro, M. López-
705 Puertas, and W. E. Ward (2016), MIPAS observations of longitudinal oscillations in the
706 mesosphere and the lower thermosphere: Part 1. Climatology of odd-parity daily frequency
707 modes. *Atmos. Chem. Phys. Discuss.* doi:10.5194/acp-2015-1065.
708

709 Gasperini, F., J. M. Forbes, E. N. Doornbos, and S. L. Bruinsma (2015), Wave coupling between
710 the lower and middle thermosphere as viewed from TIMED and GOCE, *J. Geophys. Res. Space*
711 *Physics*, 120, 5788–5804, doi:10.1002/2015JA021300.
712

713 Hagan, M. E., and J. M. Forbes (2002), Migrating and nonmigrating diurnal tides in the middle
714 and upper atmosphere excited by tropospheric latent heat release, *J. Geophys. Res.*, 107(D24),
715 4754, doi:10.1029/2001JD001236.
716

717 Hagan, M. E., A. Maute, and R. G. Roble (2009), Tropospheric tidal effects on the middle and
718 upper atmosphere, *J. Geophys. Res. Lett.*, 114, A01302, doi:10.1029/2008JA013637.
719

720 Hagan, M. E., A. Maute, R. G. Roble, A. D. Richmond, T. J. Immel, and S. L. England (2007),
721 Connections between deep tropical clouds and the Earth's ionosphere, *Geophys. Res. Lett.*, 34,
722 L20109, doi:10.1029/2007GL030142.

723

724 Häusler, K., and H. Lühr (2009), Nonmigrating tidal signals in the upper thermospheric zonal
725 wind at equatorial latitudes as observed by CHAMP, *Ann. Geophys.*, 27(7), 2643–2652,
726 doi:10.5194/angeo-27-2643-2009.

727

728 Häusler, K., H. Lühr, M. E. Hagan, A. Maute, and R. G. Roble (2010), Comparison of CHAMP
729 and TIME-GCM nonmigrating tidal signals in the thermospheric zonal wind, *J. Geophys. Res.*,
730 115, D00I08, doi:10.1029/2009JD012394.

731

732 He, M., L. Liu, W. Wan, J. Lei, and B. Zhao (2010), Longitudinal modulation of the O/N₂
733 column density retrieved from TIMED/GUVI measurement, *Geophys. Res. Lett.*, 37, L20108,
734 doi:10.1029/2010GL045105.

735

736 Hitchman, M. H. and C. B. Leovy (1985), Diurnal Tide in the Equatorial Middle Atmosphere as
737 Seen in LIMS Temperatures, *Journal of Atmospheric Sciences*, 42(6), 557-561,
738 [https://doi.org/10.1175/1520-0469\(1985\)042,0557:DTITEM>2.0.CO;2](https://doi.org/10.1175/1520-0469(1985)042,0557:DTITEM>2.0.CO;2).

739

740 Immel, T. J., E. Sagawa, S. L. England, S. B. Henderson, M. E. Hagan, S. B. Mende, H. U. Frey,
741 C. M. Swenson, and L. J. Paxton (2006), Control of equatorial ionospheric morphology by
742 atmospheric tides, *Geophys. Res. Lett.*, 33, L15108, doi:10.1029/2006GL026161.

743

744 Jones Jr., M., J. M. Forbes, M. E. Hagan, and A. Maute (2013), Non-migrating tides in the
745 ionosphere-thermosphere: In situ versus tropospheric sources, *J. Geophys. Res. Space Physics*,
746 118, 2438–2451, doi:10.1002/jgra.50257.

747

748 Jones, M., Jr., J. M. Forbes, M. E. Hagan, and A. Maute (2014), Impacts of vertically
749 propagating tides on the mean state of the ionosphere-thermosphere system, *J. Geophys. Res.*
750 *Space Physics*, 119, 2197–2213, doi:10.1002/2013JA019744.

751

752 Kil, H., W. K. Lee, J. Shim, L. J. Paxton, and Y. Zhang (2013), The effect of the 135.6 nm
753 emission originated from the ionosphere on the TIMED/GUVI O/N₂ ratio, *J. Geophys. Res.*
754 *Space Physics*, 118, 859–865, doi:10.1029/2012JA018112.

755

756 Kil, H., and L. J. Paxton (2011), The origin of the nonmigrating tidal structure in the column
757 number density ratio of atomic oxygen to molecular nitrogen, *Geophys. Res. Lett.*, 38, L19108,
758 doi:10.1029/2011GL049432.

759

760 Lewis, R. M., V. Torczon, M. W. Trosset (2000), Direct search methods: then and now, *Journal*
761 *of Computational and Applied Mathematics*, 124, 191-207, doi:10.1016/S0377-0427(00)00423-
762 4.

763

764 Li, X., W. Wan, Z. Ren, L. Liu, and B. Ning (2015), The variability of nonmigrating tides
765 detected from TIMED/SABER observations, *J. Geophys. Res. Space Physics*, 120, 10,793–
766 10,808, doi:10.1002/2015JA021577.

767

768 Lieberman, R. S. (1991), Nonmigrating diurnal tides in the equatorial middle atmosphere, *J.*
769 *Atmos. Sci.*, 48, 1112-1123, doi:10.1175/1520-0469(1991)048<1112:NDTITE>2.0.CO;2.

770

771 Lieberman, R. S., J. Oberheide, M. E. Hagan, E. E. Remsberg and L. L. Gordley (2004),
772 Variability of diurnal tides and planetary waves during November 1978–May 1979, *J. Atmos*
773 *Solar-Terrestrial Phys*, 66, 517–528, <https://doi.org/10.1016/j.jastp.2004.01.006>.

774

775 Lieberman, R. S., J. Oberheide, and E. R. Talaat (2013), Nonmigrating diurnal tides observed in
776 global thermospheric winds, *J. Geophys. Res. Space Physics*, 118, 7384–7397,
777 doi:10.1002/2013JA018975.

778

779 Maute, A. (2017). Thermosphere-ionosphere-electrodynamics general circulation model for the
780 ionospheric connection explorer: TIEGCM-ICON. *Space Science Reviews*, 212(1-2), 523–551.
781 <https://doi.org/10.1007/s11214-017-0330-3>.

782

783 McClintock, W. E., Eastes, R. W., Hoskins, A. C., Siegmund, O. H. W., McPhate, J. B.,
784 Krywonos, A., et al. (2020a). Global-scale observations of the limb and disk mission

785 implementation: 1. Instrument design and early flight performance. *Journal of Geophysical*
786 *Research: Space Physics*, 125, e2020JA027797. <https://doi.org/10.1029/2020JA027797>.

787

788 McClintock, W. E., Eastes, R. W., Beland, S., Bryant, K. B., Burns, A. G., Correira, J., et al.
789 (2020b). Global-scale observations of the limb and disk mission implementation: 2.

790 Observations, data pipeline, and level 1 data products. *Journal of Geophysical Research: Space*
791 *Physics*, 125, e2020JA027809. <https://doi.org/10.1029/2020JA027809>.

792

793 Nischal, N., Oberheide, J., Mlynczak, M. G., Marsh, D. R., & Gan, Q. (2019). Solar cycle
794 variability of nonmigrating tides in the 5.3 and 15 μm infrared cooling of the thermosphere (100–
795 150 km) from SABER. *Journal of Geophysical Research: Space Physics*, 124, 2338–2356.
796 <https://doi.org/10.1029/2018JA026356>.

797

798 Oberheide, J., J. M. Forbes, X. Zhang, and S. L. Bruinsma (2011), Climatology of upward
799 propagating diurnal and semidiurnal tides in the thermosphere, *J. Geophys. Res.*, 116, A11306,
800 doi:10.1029/2011JA016784.

801

802 Oberheide, J., M. E. Hagan, R. G. Roble, and D. Offermann (2002), Sources of nonmigrating
803 tides in the tropical middle atmosphere, *J. Geophys. Res.*, 107(D21), 4567,
804 doi:10.1029/2002JD002220.

805

806 Oberheide, J., M. G. Mlynczak, C. N. Mosso, B. M. Schroeder, B. Funke, and A. Maute (2013),
807 Impact of tropospheric tides on the nitric oxide 5.3 μm infrared cooling of the low-latitude

808 thermosphere during solar minimum conditions, *J. Geophys. Res. Space Physics*, 118, 7283–
809 7293, doi:10.1002/2013JA019278.

810

811 Oberheide, J., Pedatella, N. M., Gan, Q., Kumari, K., Burns, A. G., & Eastes, R. (2020).
812 Thermospheric composition O/N₂ response to an altered meridional mean circulation during
813 Sudden Stratospheric Warmings observed by GOLD. *Geophysical Research Letters*, 47,
814 e2019GL086313. <https://doi.org/10.1029/2019GL086313>.

815

816 Pedatella, N. M., J. M. Forbes, A. Maute, A. D. Richmond, T.-W. Fang, K. M. Larson, and G.
817 Millward (2011), Longitudinal variations in the F region ionosphere and the topside ionosphere-
818 plasmasphere: Observations and model simulations, *J. Geophys. Res.*, 116, A12309,
819 doi:10.1029/2011JA016600.

820

821 Pedatella, N. M., J. Oberheide, E. K. Sutton, H.-L. Liu, J. L. Anderson, and K. Raeder (2016),
822 Short-term nonmigrating tide variability in the mesosphere, thermosphere, and ionosphere, *J.*
823 *Geophys. Res. Space Physics*, 121, 3621–3633, doi:10.1002/2016JA022528.

824

825 Strickland, D. J., J. S. Evans, and L. J. Paxton (1995), Satellite remote sensing of thermospheric
826 O/N₂ and solar EUV: 1. Theory, *J. Geophys. Res.*, 100, 12,217–12,226, doi:10.1029/95JA00574.

827

828 Wallace, J. M., and F. R. Hartranft (1969), Diurnal wind variations, surface to 30 km, *Mon. Wea.*
829 *Rev.*, 97, 446–455, doi:10.1175/1520-0493(1969)097<0446:DWVSTK>2.3.CO;2.

830

831 Wallace, J. M., and R. F. Tadd (1974), Some further results concerning the vertical structure of
832 atmospheric tidal motions within the lowest 30 kilometers, *Mon. Wea. Rev.*, 102, 795–803,
833 doi:10.1175/1520-0493(1974)102<0795:SFRCTV>2.0.CO;2.

834

835 Ward, W. E., et al. (2010), On the consistency of model, ground-based, and satellite observations
836 of tidal signatures: Initial results from the CAWSES tidal campaigns, *J. Geophys. Res.*, 115,
837 D07107, doi:10.1029/2009JD012593.

838

839 Ward, W. E., Oberheide, J., Riese, M., Preusse, P., and Offermann, D. (1999), Tidal signatures in
840 temperature data from CRISTA 1 mission, *J. Geophys. Res.*, 104(D13), 16391– 16403,
841 doi:10.1029/1998JD100109.

842

843 Zhang, X., J. M. Forbes, and M. E. Hagan (2010a), Longitudinal variation of tides in the MLT
844 region: 1. Tides driven by tropospheric net radiative heating, *J. Geophys. Res.*, 115, A06316,
845 doi:10.1029/2009JA014897.

846

847 Zhang, X., J. M. Forbes, and M. E. Hagan (2010b), Longitudinal variation of tides in the MLT
848 region: 2. Relative effects of solar radiative and latent heating, *J. Geophys. Res.*, 115, A06317,
849 doi:10.1029/2009JA014898.

850

851 Zhang, X., J. M. Forbes, M. E. Hagan, J. M. Russell III, S. E. Palo, C. J. Mertens, and M. G.
852 Mlynczak (2006), Monthly tidal temperatures 20–120 km from TIMED/SABER, *J. Geophys.*
853 *Res.*, 111, A10S08, doi:10.1029/2005JA011504.